GEOPHYSICS, VOL. 73, NO. 2 (MARCH-APRIL 2008); P. R37–R48, 22 FIGS.
10.1190/1.2838274

Layer-thickness determination and stratigraphic interpretation using spectral inversion: Theory and application

Charles I. Puryear[1] and John P. Castagna[1]

ABSTRACT

Spectral inversion is a seismic method that uses a priori information and spectral decomposition to improve images of thin layers whose thicknesses are below the tuning thickness. We formulate a method to invert frequency spectra for layer thickness and apply it to synthetic and real data using complex spectral analysis. Absolute layer thicknesses significantly below the seismic tuning thickness can be determined robustly in this manner without amplitude calibration. We extend our method to encompass a generalized reflectivity series represented by a summation of impulse pairs. Application of our spectral inversion to seismic data sets from the Gulf of Mexico results in reliable well ties to seismic data, accurate prediction of layer thickness to less than half the tuning thickness, and improved imaging of subtle stratigraphic features. Comparisons between well ties for spectrally inverted data and ties for conventional seismic data illustrate the superior resolution of the former. Several stratigraphic examples illustrate the various destructive effects of the wavelet, including creating illusory geologic information, such as false stratigraphic truncations that are related to lateral changes in rock properties, and masking geologic information, such as updip limits of thin layers. We conclude that data that are inverted spectrally on a trace-by-trace basis show greater bedding continuity than do the original seismic data, suggesting that wavelet side-lobe interference produces false bedding discontinuities.

INTRODUCTION

According to the Widess (1973) model, seismically thin layers below one-eighth of a wavelength in thickness cannot be resolved. However, such thin layers might be significant reservoirs or important flow units within reservoirs. Exploration and development geophysicists frequently are faced with the task of inferring layer thickness for layers such as these where the top and base of the layer cannot be mapped distinctly. Consequently, determining layer properties for such seismically thin beds is of great interest in exploration and development applications.

Although tuning-thickness analysis based on the theory of Widess (1973) and Kallweit and Wood (1982) has been the thickness-mapping method of choice for several decades, Partyka et al. (1999), Partyka (2005), and Marfurt and Kirlin (2001) demonstrate the effectiveness of spectral decomposition using the discrete Fourier transform (DFT) as a thickness-estimation tool. However, such methods have difficulty with thin layers if seismic bandwidth is insufficient to identify the periodicity of spectral peaks and notches unambiguously. This difficulty motivates the development of methods that do not require precise identification of peaks and troughs within the seismic bandwidth.

Partyka (2005), Portniaguine and Castagna (2004, 2005), Puryear (2006), Chopra et al. (2006a, 2006b), and Puryear and Castagna (2006) show that inversion of spectral decompositions for layer properties can be improved when reflection coefficients are determined simultaneously. The result is a sparse-reflectivity inversion that can be parameterized to provide robust layer-thickness estimates. Such a process, called spectral inversion, produces results that differ from conventional seismic inversion methods.

In this article, we discuss the basic theory of spectral inversion, develop a new spectral-inversion algorithm, and show field examples of improved bed-thickness determination and enhanced stratigraphic imaging that can be achieved with the process.

Widess model

The Widess (1973) model for thin-bed reflectivity teaches that the fundamental limit of seismic resolution is $\lambda/8$, where λ is the wavelength. Essentially, constructive wavelet interference and measured amplitude in the time domain peak at $\lambda/4$. The waveform shape and peak frequency continue to change somewhat as amplitude decreases to $\lambda/8$, at which point the waveform approximates the derivative of the seismic wavelet. As the layer thins below $\lambda/8$, the waveform

Manuscript received by the Editor 18 April 2007; revised manuscript received 31 October 2007; published online 27 February 2008.
[1]University of Houston, Department of Geosciences, Houston, Texas, U.S.A. E-mail: cipuryear@hotmail.com; jcastagnaou@yahoo.com.
© 2008 Society of Exploration Geophysicists. All rights reserved.

Downloaded 02 Sep 2010 to 98.201.156.213. Redistribution subject to SEG license or copyright; see Terms of Use at http://segdl.org/

does not change significantly, but amplitude steadily decreases, as demonstrated in Figure 1. In this figure, amplitudes are obtained from the convolution of a 30-Hz Ricker wavelet with a wedge model.

From this point of view, there are no means to differentiate between amplitude changes associated with reflection-coefficient changes and thickness changes below $\lambda/8$, making this thickness a hard resolution limit for broadband analysis in the time domain. Worse yet, in the presence of noise and wavelet broadening, the transition between $\lambda/4$ and $\lambda/8$ is obscured, sometimes making $\lambda/4$ a practical limit of resolution. The key assumptions for the Widess model are that the half-spaces above and below the layer of interest have the same acoustic impedance and that the acoustic impedance of the thin layer is constant.

Generalized reflectivity model

Although the theory of Widess (1973) is valid when the assumptions are satisfied, nature rarely accommodates such strict theoretical provisions. The theory of spectral inversion is based on the realization that the Widess model for thin-bed reflectivity presupposes a reflectivity configuration that is actually a singularity in the continuum of possible reflection-coefficient ratios. Any reflection-coefficient pair can be decomposed into even and odd components, with the even components having equal magnitude and sign and the odd components having equal magnitude and opposite sign, as described by Castagna (2004) and Chopra et al. (2006a, b).

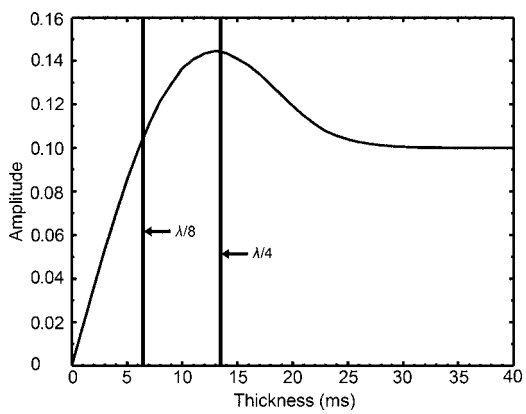

Figure 1. Plot of amplitude versus thickness. Note the increase in amplitude over background as the tuning thickness ($\lambda/4$) is approached. Below tuning, the amplitude rolls off nearly linearly, and the waveform approximates the derivative of the wavelet at $\lambda/8$.

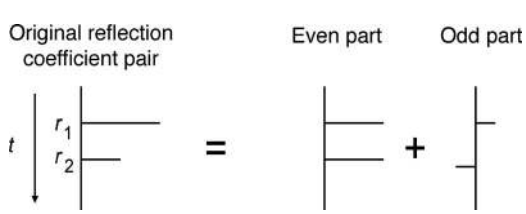

Figure 2. Any arbitrary pair of reflection coefficients r_1 and r_2 can be represented as the sum of even and odd components. The even pair has the same magnitude and sign, and the odd pair has the same magnitude and opposite sign.

The identity is illustrated in Figure 2. The Widess model assumes that reflection-coefficient pairs are perfectly odd, which can be a good approximation for certain target classes such as a sand layer encased in a shale matrix. However, the assumption of an odd-reflectivity pair implies the worst possible resolution for thin beds. Even a small even component in the reflection-coefficient pair can increase the resolvability of a layer significantly. The improvement in resolution results from the fact that the even component constructively interferes as thickness approaches zero. In contrast, the odd component destructively interferes. Thus, the even component is more robust against noise as thickness approaches zero (see Tirado, 2004).

We calculated peak frequency and peak amplitude from equations given by Chung and Lawton (1995). Figure 3a shows the effect of thinning on the peak frequency of a reflection-coefficient pair with even and odd components. For the model, the total peak frequency increases with decreasing thickness and then returns to the peak frequency of the wavelet rather than that of the derivative of the wavelet as predicted by the Widess model. Interestingly, the total peak frequency shows significant and continuous change down to zero thickness. Likewise, the total peak amplitude (Figure 3b) does not approach zero with thickness as predicted by the Widess model.

The example indicates that the reflection-amplitude trend can show significant variation from the Widess curve (Figure 1) as the layer thickness approaches zero when the even component is nonzero. Thus, significant information below the Widess resolution limit is not captured by traditional amplitude-mapping techniques, which assume equal and opposite reflection coefficients. Such examples of unequal reflection coefficients at the top and base of a layer, which are the rule rather than the exception for most real-world seismic reflections events, reinforce the need for a more generalized approach to thin-bed amplitude analysis.

Based on the fact that spacing between spectral peaks and notches is a deterministic function of layer thickness, our objective was to develop a new algorithm to invert reflectivity using the constant periodicity in the frequency domain. Our development started with the expression for an impulse pair in the time domain, from which we

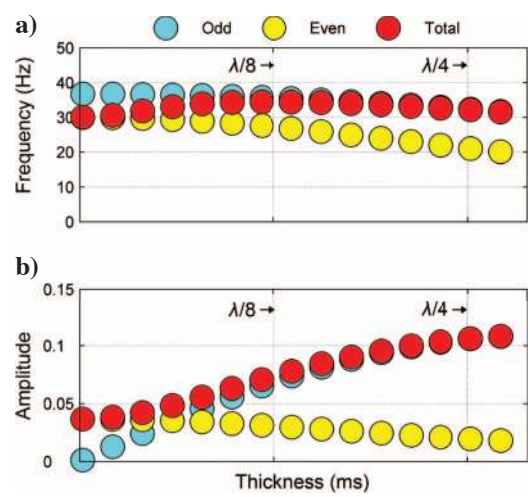

Figure 3. (a) Peak frequency and (b) peak amplitude as a function of thickness for the even component, the odd component, and the total. In (a), there is peak-frequency information below the tuning thickness. In (b), total peak amplitude approaches the even-component amplitude below tuning. Layer model parameters are $r_1 = -0.2$, $r_2 = 0.1$, and $f_0 = 30$ Hz.

Downloaded 02 Sep 2010 to 98.201.156.213. Redistribution subject to SEG license or copyright; see Terms of Use at http://segdl.org/

formulated a numerical algorithm using complex spectral analysis and then tested the algorithm on synthetic wedge models. We extended our development to multiple layers, and we tested our method on 3D seismic data from the Gulf of Mexico shelf, comparing seismic data, spectrally inverted seismic data, and well-log data.

METHODS

Spectral-inversion method

We applied windowed Fourier transforms to several reflectivity models to generate data for spectral inversion and used complex spectral analysis to formulate the inversion algorithm. The algorithm described herein defines the inversion for reflectivity using the constant periodicity of the amplitude spectrum for a layer of a given thickness, taking advantage of the fact that spacing between spectral peaks and notches is precisely the inverse of the layer thickness in the time domain (Partyka et al., 1999; Marfurt and Kirlin, 2001). Essentially, layer thickness can be determined robustly from a narrow band of frequencies with a high signal-to-noise ratio (S/N). To prove this concept, note that the entire reflectivity spectrum for a single layer could be reconstructed from amplitudes at three frequencies in the absence of noise.

Beginning with the expression for an impulse pair in the time domain as expressed by Marfurt and Kirlin (2001) (Figure 4),

$$g(t) = r_1\delta(t - t_1) + r_2\delta(t - t_1 - T), \tag{1}$$

where r_1 is the top reflection coefficient, r_2 is the base reflection coefficient, t is a time sample, t_1 is a time sample at the top reflector, and T is layer thickness. Locating the analysis point at the center of the layer yields

$$g(t) = r_1\delta\left(t - \frac{T}{2}\right) + r_2\delta\left(t + \frac{T}{2}\right). \tag{2}$$

Taking the Fourier transform of the shifted expression 2 gives

$$g(t,f) = r_1 \exp\left[-i2\pi f\left(t - \frac{T}{2}\right)\right] + r_2 \exp\left[-i2\pi f\left(t + \frac{T}{2}\right)\right], \tag{3}$$

where f is frequency and $g(f)$ is the complex spectrum. Simplifying by using trigonometric identities and taking the real part yields

$$\mathrm{Re}[g(f)] = (2r_e)\cos(\pi f T), \tag{4}$$

where r_e is the even component of the reflection-coefficient pair. Similarly, the imaginary part of the complex spectrum is

$$\mathrm{Im}[g(f)] = (2r_o)\sin(\pi f T), \tag{5}$$

where r_o is the odd part of the reflection-coefficient pair.

Figure 5 shows plots for both the even and odd reflectivity spectra corresponding to equations 4 and 5 for a layer with thickness $T = 10$ ms and reflection coefficients $r_1 = 0.2$ and $r_2 = 0.1$. Although both even and odd spectra show the same notch period, the two are shifted by half of the frequency spacing. For the individual real and imaginary components, the constant period in the spectrum is related to the symmetrical location of the analysis point at the center of the layer. This placement effectively divides the reflection-coefficient pair into perfectly odd and even components, thereby eliminating the phase variation for each. The effect of violating this condition is discussed in Appendix A.

To maintain constant periodicity in the spectrum while shifting the analysis point away from the layer center, we compute the modulus of the real and imaginary components of the spectrum, which is insensitive to phase. Beginning with general expressions for the real and imaginary time-shifted spectra,

$$\mathrm{Im}[e^{2i\pi f\Delta t}g(f)] = 2r_o\sin(\pi f T)\cos(2\pi f\Delta t) + 2r_e\cos(\pi f T)\sin(2\pi f\Delta t) \tag{6}$$

and

$$\mathrm{Re}[e^{2i\pi f\Delta t}g(f)] = 2r_e\cos(\pi f T)\cos(2\pi f\Delta t) - 2r_o\sin(\pi f T)\sin(2\pi f\Delta t), \tag{7}$$

it can be shown (Appendix B) that

$$O(t,k) = G(f)\frac{dG(f)}{df} + 2\pi T k\sin(2\pi f T), \tag{8}$$

where $G(f)$ is amplitude magnitude as a function of frequency, $k = r_e^2 - r_o^2$, and $O(t,k)$ is the cost function at each frequency. The so-

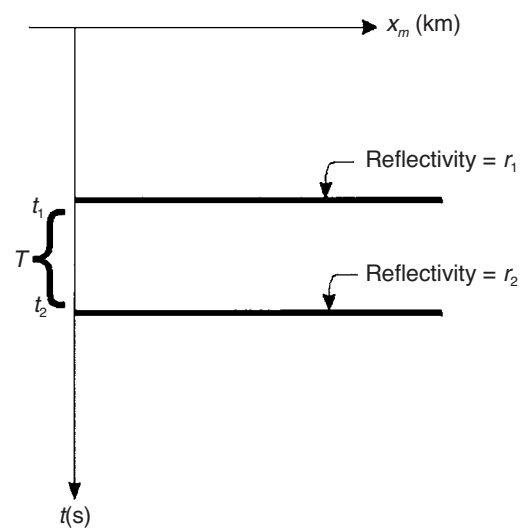

Figure 4. Two-layer reflectivity model (from Marfurt and Kirlin, 2001).

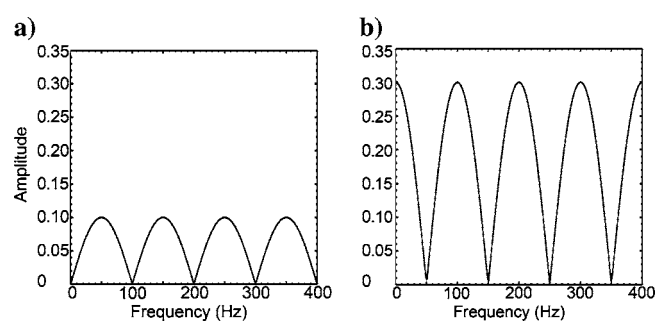

Figure 5. Amplitude versus frequency plots for (a) even and (b) odd components of the reflection-coefficient pair $r_1 = 0.2$ and $r_2 = 0.1$. In this example, the even component is dominant.

Downloaded 02 Sep 2010 to 98.201.156.213. Redistribution subject to SEG license or copyright; see Terms of Use at http://segdl.org/

lution to equation 8 occurs when the sum of cost functions $O(t,k)$, evaluated at each frequency, is minimized over the range of frequencies within the analysis band. One data term exists at every sample frequency, so the performance of the method is determined by the S/N over a given analysis band (i.e., more frequencies with a high S/N yield a more stable and accurate inversion).

We found the global minimum of equation 8 for a given analysis band by searching physically reasonable model parameters k and T in two-parameter model space and minimizing the objective function (Figure 6). Although it is costly and impractical for more complicated cases, the global search method guarantees the avoidance of local minima for the single-layer case. The remaining model parameters then are determined by

$$r_o = \sqrt{\frac{G(f)^2}{4} - k\cos^2(\pi f T)}, \tag{9}$$

$$r_e = \sqrt{k + r_o^2}, \tag{10}$$

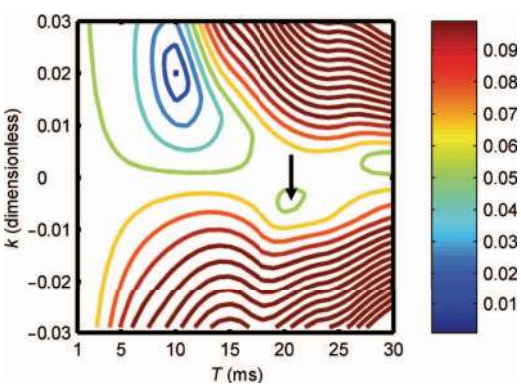

Figure 6. The difference or error function between the data and a range of model parameter pairs is calculated. The blue bull's-eye is the correct model solution ($T = 10$ ms, $k = 0.02$). The black arrow shows a local minimum.

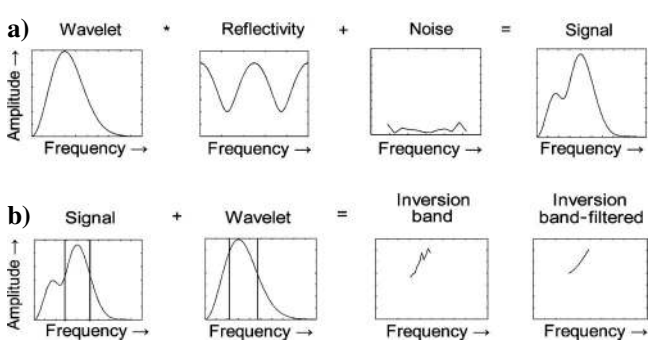

Figure 7. (a) Forward-model and (b) inverse-model schemes used for the synthetic. The plots show magnitude of amplitude versus frequency. In (a), multiplication of the wavelet with the reflectivity spectrum and addition of noise in the frequency domain yields the seismic signal. In (b), division of the seismic signal by the wavelet in the frequency domain yields the noisy reflectivity band. A smoothing filter produces the inversion band for input to the model.

and

$$t_1 = \frac{1}{2i\pi f}\ln\left[\frac{g(f)}{r_1 + r_2 e^{2i\pi f T}}\right], \tag{11}$$

where t_1 is the time sample at the top reflector r_1 and $g(f)$ is the complex spectrum for the reflection-coefficient pair. Equation 11 can be derived by taking the Fourier transform of equation 1 and solving for t_1. The reflection coefficients r_1 and r_2 can be recovered by recomposing the odd and even components of the pair calculated using equations 9 and 10, the reverse of the operation illustrated in Figure 2. Thus, it is straightforward to compute the remaining components of the layer-reflectivity model from the initial parameters k and T. Note that although the derivation (Appendix B) of the algorithm assumes that the even reflectivity component is greater than the odd reflectivity component, the solution is the same for the antithetical assumption.

Modeling results

We test the method by convolving a 30-Hz Ricker wavelet with reflection-coefficient pairs that have various ratios. We produce wedge models with 4-ms sampling for a predominantly odd reflection-coefficient pair, $r_1 = -0.2$ and $r_2 = 0.1$, and a predominantly even reflection-coefficient pair, $r_1 = 0.2$ and $r_2 = 0.1$. The tuning thickness of a thin-bed model with a Ricker wavelet is given by Chung and Lawton (1995):

$$t_R = \frac{\sqrt{6}}{2\pi f_0}, \tag{12}$$

where f_0 is the dominant wavelet frequency. For a 30-Hz Ricker wavelet, $t_R = 13$ ms. The convolution of the wavelet with the reflection-coefficient pair in the time domain is equivalent to multiplication with the reflectivity spectrum in the frequency domain. The inversion performs perfectly in the absence of noise for layers of any thickness.

To achieve a more realistic model, we added noise in the time domain, and we measured and controlled the noise level by computing the ratio of the area under the spectrum of the signal to that of the noise in the frequency domain. We tested the model with 1% and 5% noise levels. The forward-modeling procedure is illustrated in Figure 7a.

The addition of noise causes instability in the inversion for very thin layers, partly because the reflectivity spectrum approaches a flat spectrum as T approaches zero. We mitigated this problem by applying the arbitrary constraint $-0.03 < k < 0.03$ to ensure that the reflection-coefficient strength could not exceed what typically is observed in seismograms. After Fourier-transforming the time-domain signal, we removed the wavelet overprint by dividing the magnitude of the amplitude of the seismic signal by that of the wavelet at each analysis frequency.

We tested the inversion at different noise levels while varying the analysis band and smoothing filter. These experiments showed that the optimal analysis band and the optimal smoothing filter are determined by the noise level. We achieved optimal results for the 1% noise case using a 25-Hz bandwidth sampled at 2-Hz frequency increments and centered on the peak signal frequency. A signal is corrupted by noise, so it was necessary to narrow the bandwidth. For the 5% noise case, we achieved optimal results with a 20-Hz bandwidth.

Downloaded 02 Sep 2010 to 98.201.156.213. Redistribution subject to SEG license or copyright; see Terms of Use at http://segdl.org/

More smoothing is required to stabilize the derivative operator as noise is added. The process resulting in the smoothed inversion band is illustrated in Figure 7b. We took derivatives of the magnitude of the amplitude with respect to frequency at each observation frequency sample using a first-order central difference approximation. Finally, we multiplied the magnitude of the amplitude at each observation frequency by the derivative of the magnitude of the amplitude at that frequency and minimized the error between the model defined by equation 8 and the data for the range of frequencies within the analysis band (Figure 6).

We applied the inversion defined by equation 8 using a 256-ms-window fast Fourier transform (FFT) for spectral decomposition to wedge models that have predominantly odd and even reflection-coefficient pairs (Figure 8). Figure 9a and b shows the result of the inversion (black) compared with the true reflectivity model (green and red) for 1% and 5% levels of noise, respectively, for the predominantly odd reflection-coefficient pair; Figure 9c and d shows these results for the predominantly even pair. The tuning thickness is represented by the vertical black line.

We compared the 5% noise results with the corresponding amplitude-mapping results (brown) using tuning analysis (Widess, 1973; Kallweit and Wood, 1982). The algorithm performed nearly perfectly for both configurations at 1% noise levels as expected, illustrating the principle that noiseless data could yield extremely high resolution.

Although the noise level is unrealistically low for most seismic data, the results highlight the importance of meticulous noise suppression during acquisition and processing. For thin layers, the results are useful far below tuning. For the 5% noise cases, the absolute error does not increase significantly for very thin layers because of the reflectivity constraint, although the percent error increases as layer thickness decreases. Reflection-coefficient estimates were comparably accurate. As expected, accuracy deteriorates as noise increases beyond 5%. Thus, for a given wavelet peak frequency and analysis band, noise level rather than tuning thickness determines the limit of resolution.

The tuning-analysis predictions are shifted toward thicker layers for the even and odd components because of the assumption of equal-magnitude reflection coefficients at the top and base. The assumption in the relationship between amplitude and thickness depends on the particular mapping scheme. We plotted the results of the amplitude-mapping techniques that generated the least error in thickness prediction. For the predominantly odd pair, the optimal amplitude-mapping method was a simple linear regression from peak tuning to zero thickness. However, this technique generated large errors and negative thickness predictions for the predominantly even pair. So for the predominantly even pair, we assumed both of the reflection coefficients were equal to the peak background amplitude for the thick layer and mapped thickness from the tuning amplitude to zero thickness.

We tested the inversion on a reflector model that violates the basic assumptions of the method. The model includes two layers defined by three reflectors, all with reflection coefficients equal to 0.1. The top layer has twice the thickness of the lower layer. We decomposed the spectrum using an 80-ms DFT with a Gaussian taper centered on the thicker layer.

Figure 10 shows the model (green and red) and the resulting inversion (black). The predicted layer thickness is measured from the top reflector to the black line, yielding a thickness value greater than that of the thicker layer but less than that of the two layers combined. The observed predicted thickness results from the interference of the two layers in the frequency domain, creating a period corresponding to a single layer that is slightly thicker than the thickest layer. The reflection-coefficient predictions for the lower reflector are closer to the sum of the two base reflection coefficients $r_2 + r_3 = 0.2$ for thin layers and to the single base reflection-coefficient value $r_2 = r_3 = 0.1$ for thicker layers. In practice, additional spikes widely spaced from the reflectors of the layer should be considered noise for the single-layer model.

Although we value the single-layer model for its ease of invertibility, it is necessary to extend the inversion scheme so that it simultaneously can invert seismograms containing multiple interfering layers for most real cases.

Extension of the method to multiple layers

Recognizing that a seismogram can be represented as a superposition of impulse pairs, the inversion for the properties of a single layer is extended easily to encompass a general reflectivity-series inversion by considering the spectrum versus time acquired using a moving window as a superposition of interference patterns originating at different times. The inversion process for reflection coefficients and layer thickness is performed simultaneously for all impulse pairs affecting the local seismic response.

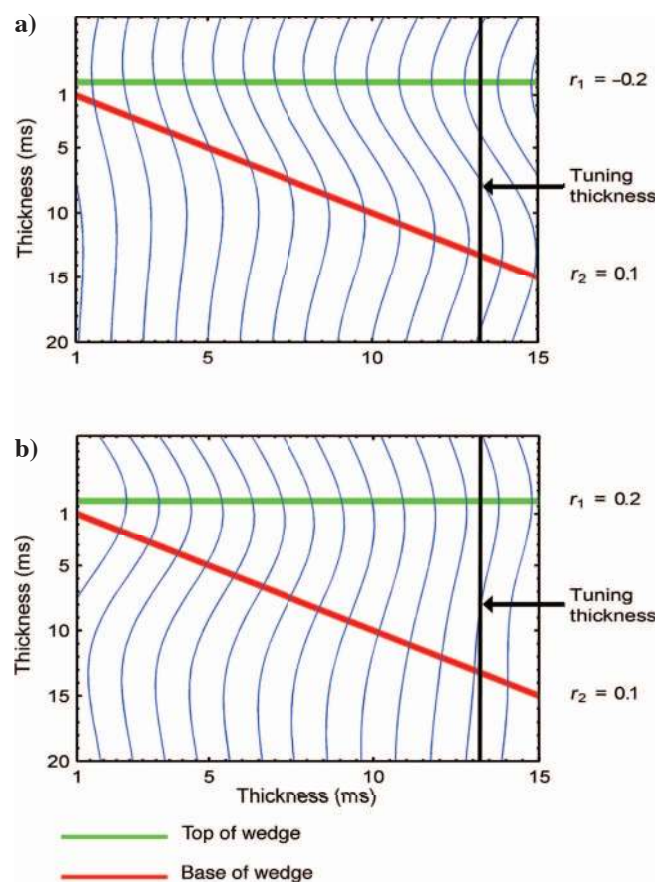

Figure 8. Original reflectivity wedge models for (a) a predominantly odd reflection-coefficient pair and (b) a predominantly even reflection-coefficient pair. The vertical black line defines the tuning thickness for the 30-Hz Ricker wavelet convolved with the reflection-coefficient pair (blue).

Downloaded 02 Sep 2010 to 98.201.156.213. Redistribution subject to SEG license or copyright; see Terms of Use at http://segdl.org/

Let us represent the reflectivity series $r(t)$ as a summation of even and odd impulse pairs:

$$r(t) = \int_{-\infty}^{\infty} \left[r_e(t) II\left(\frac{t-\tau}{T(t)}\right)\right] dt + \int_{-\infty}^{\infty} \left[r_o(t) I_I\left(\frac{t-\tau}{T(t)}\right)\right] dt, \tag{13}$$

where $r_e(t)$ and $r_o(t)$ are the magnitudes of the impulse pairs as a function of time, $T(t)$ is the time series of layer time thicknesses, I_I is an odd impulse pair, and II is an even impulse pair. Assuming a convolutional seismogram and known wavelet $w(t,f)$, a spectral decomposition of a seismic trace $s(t,f)$ is then

$$s(t,f) = w(t,f) \int_{-t_w}^{t_w} \{r_e(t)\cos[\pi f T(t)] + i r_o(t)\sin[\pi f T(t)]\} dt, \tag{14}$$

where t_w is window half-length. The multilayer case involves more than two reflectors, so it is necessary to use an objective function for inversion that properly accounts for interference between multiple layers.

If the wavelet spectrum is known, we can solve for $r(t)$ and $T(t)$ by optimizing the objective function $O(t, r_e, r_o, T)$ by

$$O(t,r_e,r_o,T) = \int_{f_L}^{f_H} \left[\alpha_e \left\{ \mathrm{Re}[s(t,f)/w(t,f)] - \int_{-t_w}^{t_w} r_e(t)\cos[\pi f T(t)] dt \right\} + \alpha_o \left\{ \mathrm{Im}[s(t,f)/w(t,f)] - \int_{-t_w}^{t_w} r_o(t)\sin[\pi f T(t)] dt \right\} \right] df, \tag{15}$$

where f_l is low-frequency cutoff, f_h is high-frequency cutoff, and α_e and α_o are weighting functions, the ratio of which can be adjusted to find an acceptable trade-off between noise and resolution. For high α_o/α_e, the reflectivity approaches the Widess model, and the resolution limit becomes $\lambda/8$. We summarize the multilayer inversion process in Figure 11.

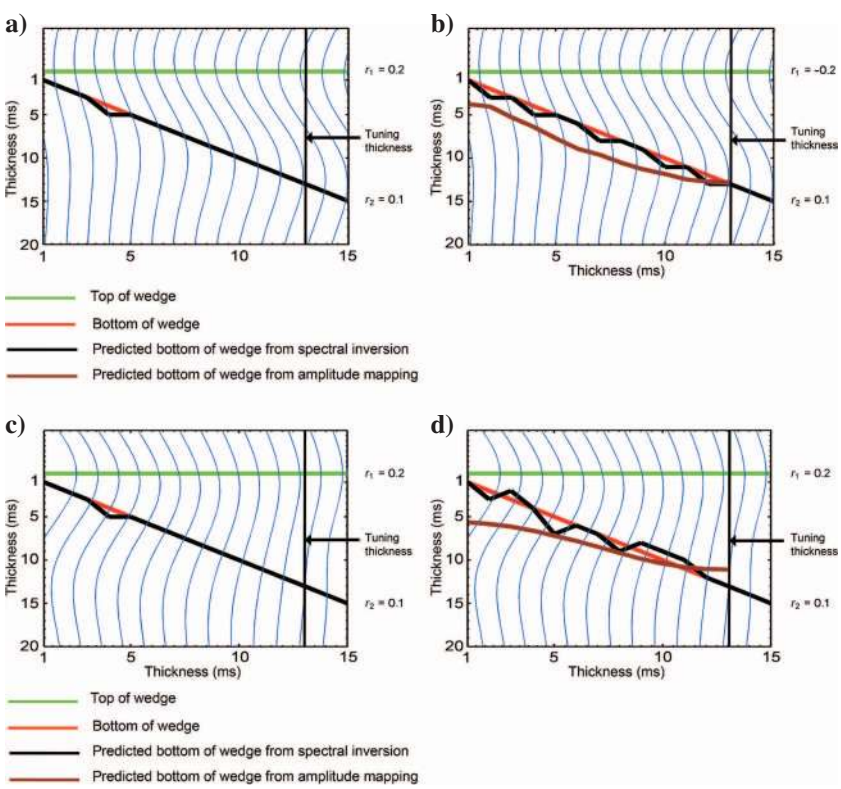

Figure 9. Result of the thickness inversion of a predominantly odd reflection-coefficient pair with (a) 1% noise and (b) 5% noise and a predominantly even reflection-coefficient pair, also with (c) 1% noise and (d) 5% noise. The plot shows the original model (green and red) along with the inversion (black) and the amplitude-mapping technique (brown), which uses the incorrect assumption of equal reflectivity. The vertical black line defines the tuning thickness for the 30-Hz Ricker wavelet convolved with the reflection-coefficient pair (blue).

Multilayer synthetic example

To validate the multilayer inversion technique in a controlled situation, we generated a model containing several arbitrary layers (Figure 12a), from which we generated a synthetic trace (Figure 12b). The reflectivity spikes were convolved with a 30-Hz Ricker wavelet. The identical trace with variable random noise is repeated in Figure 12 for clarity. We tested the inversion using windows of different lengths and centered at different locations along the synthetic trace. Assuming no a priori insight, we set the weighting function relationship $\alpha_o = \alpha_e$ and minimized the objective function given by equation 15 using a standard least-squares conjugate-gradient inversion.

We inverted the data from a 200-ms Gaussian-tapered Fourier transform, thereby recovering the original model (Figure 12c). Shortening the total window length to 100 ms and maintaining the Gaussian taper, we computed the Fourier transform for time samples between 50 and 150 ms, respectively. The window was shifted one time sample at a time, with the results of each previous window acting as a constraint for the next inversion. If no new reflectors appeared in the window or exited the window as it shifted downward, the result was the same as in the previous window. If there were no reflectors in the window, the algorithm inverted the noise, a result that was not particularly problematic because the noise was not amplified.

Downloaded 02 Sep 2010 to 98.201.156.213. Redistribution subject to SEG license or copyright; see Terms of Use at http://segdl.org/

The results for the windows centered at 50 and 150 ms are shown in Figure 12d and e. As expected, the shorter windows divide the overall longer series of reflectors into two isolated sets. By superposition, we can sum the two sets of reflectors to obtain the longer series. Although the window length can be varied according to the desired result, there are practical limits to the length of an optimal inversion window, which often are defined by trial and error. If the window is too short, frequency resolution suffers; if the window is too long, time resolution is lost (see Castagna et al., 2003).

REAL DATA RESULTS

Comparison to well-log data

We studied the results of the application of the multilayer spectral-inversion process (Figure 11) to two seismic data sets from the Gulf of Mexico shelf. Well information for lithologic interpretation, including P-wave, resistivity, and deep induction, was available (Figure 13). We created a synthetic tie between the input seismic data and the well-log data, stretching the well-log data to time without reference to the inverted data for an unbiased, quantitative layer-thickness comparison between the well-log data and the inverted data. The wavelet extracted from the well for the synthetic is shown in Figure 14. We also visually compared the well-log data, the inverted data, and the original data to assess the difference in vertical resolution between the inverted data and the original data (Figures 15 and 16).

In the original seismic tie to the well (Figure 13), we achieved a relatively good fit ($r = 0.64$) between the reflectivity convolved with the extracted wavelet and the seismic trace. However, because the seismic data are much lower in frequency than the log data, the fit is useful only as an approximation for aligning gross lithologic packages. A great deal of useful information is lost to the seismic wavelet.

The thickness inversion provides a significantly better representation of the layering observed in the log data than the original seismic data does. Figure 15 shows the spectral inversion for reflectivity, displayed with a $-90°$ phase shift to emphasize relative impedance changes and a slight time shift from the original synthetic to provide a tie to the well with higher fidelity. The need for this time shift be-

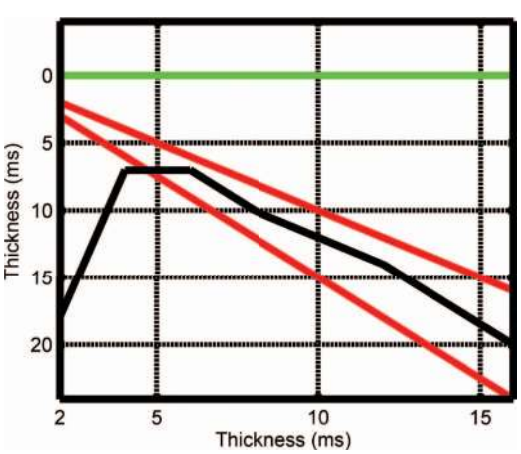

Figure 10. Result of the inversion for a two-layer model (red), violating the assumptions of the method. For thicker layers, the predicted layer thickness from the inversion (black), measured from the top reflector, falls between the thickness of the thicker layer and that of the total package. As the reflectors converge, the inversion becomes unstable.

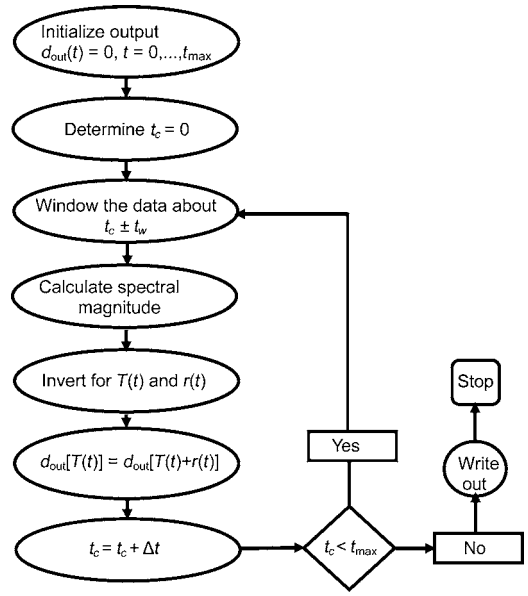

Figure 11. Flowchart for the method of the inversion, where d_{out} is the output trace, t_c is the time sample at the center of the window, and Δt is the sampling interval.

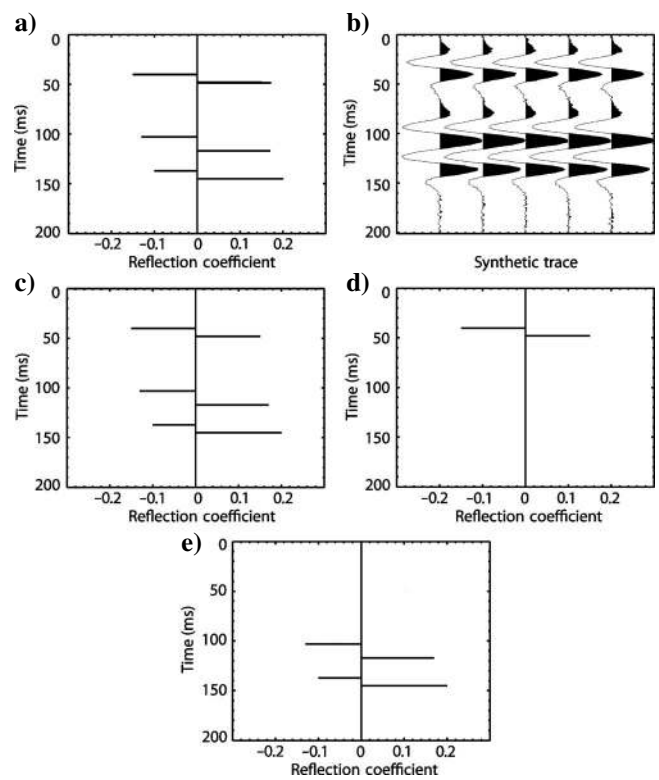

Figure 12. (a) The original model is convolved with a 30-Hz Ricker wavelet to create (b) a synthetic seismogram. (c) The spectral-inversion result using a 200-ms window centered at 100 ms recovers the original reflectivity series. (d) The spectral-inversion result using a 100-ms window centered at 50 ms and (e) the spectral-inversion result using a 100-ms window centered at 150 ms recover the portions of the reflectivity series contained within the window. By superposition, $c = d + e$.

Downloaded 02 Sep 2010 to 98.201.156.213. Redistribution subject to SEG license or copyright; see Terms of Use at http://segdl.org/

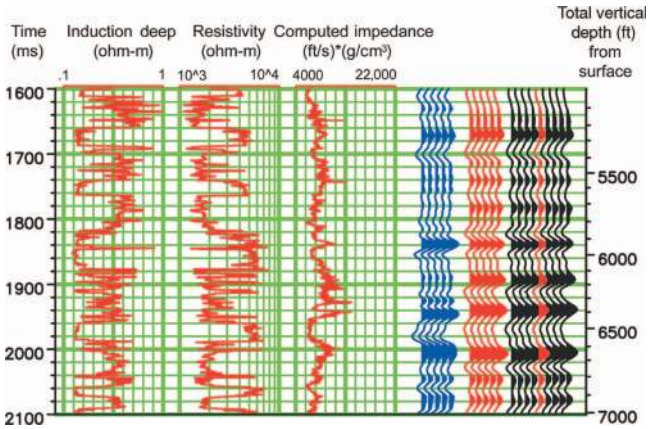

Figure 13. Well-log data, including deep induction, resistivity, and computed impedance, long with the synthetic tie (blue), the trace at the well (red), and the seismic traces surrounding the well (black). The correlation coefficient r is 0.64.

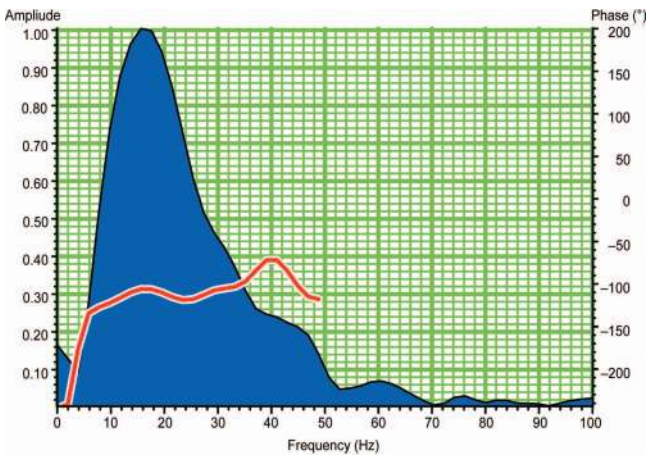

Figure 14. The phase and amplitude spectra of the wavelet extracted from the well. The peak frequency is 16 Hz.

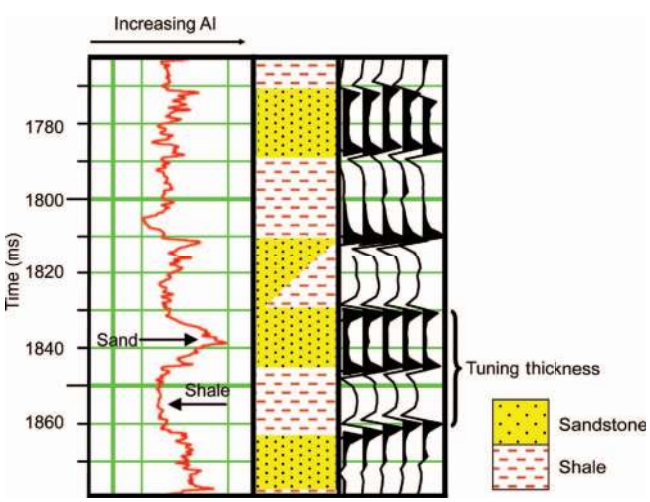

Figure 15. Impedance log (left) compared with spectrally inverted data (right). Sands are of higher impedance in this interval. The lithologic section interpreted from the impedance log shows a close correspondence to the inverted data. Note the two-layer sequence resolved at the tuning thickness.

comes apparent only after reflectivity inversion. The lithologic column shows sand and shale packages interpreted primarily from the three logs (see Figure 13). We initially distinguished sands and shales using a gamma-ray log, but we used resistivity, deep induction, and impedance for the bulk of the interpretation because gamma-ray data were absent in the well with an available P-wave velocity log.

Generally, sands correspond to higher resistivity and separation of deep induction and shallow-resistivity curves as a result of mud-filtrate invasion. In the interval shown in Figure 15, the sands have higher impedance than the shales. Comparing the lithologic column to the inverted data, the thickness inversion clearly shows layering below the tuning thickness (the peak frequency of the data is 16 Hz, yielding a one-quarter-wavelength resolution of about 31 ms). A well-resolved sand-shale sequence that has a total thickness very close to the tuning thickness is indicated also in Figure 15. Although the thickness inversion effectively delineates the layering sequence below tuning, it fails to capture gradational impedance changes within thin layers, as in the case of shale grading to sand, shown in the lithologic column.

The following example demonstrates the vast improvement in vertical resolution for discrete layers that is achieved by using thickness inversion rather than the original data.

Comparison to conventional seismic data

Viewing the comparison of the thickness inversion to the original seismic data in Figure 16, both with a $-90°$ phase rotation, it is clear that boundaries between layers are indistinct on the original seismic section. Layers below the 31-ms tuning thickness are not resolved in the original seismic data. Geologic detail is obscured by the wavelet-interference patterns, which become more apparent when compared with the inversion. A skilled interpreter can decipher meaningful information embedded in the wavelet-interference patterns, but it is desirable to remove these artifacts altogether to allow direct access to the underlying geology.

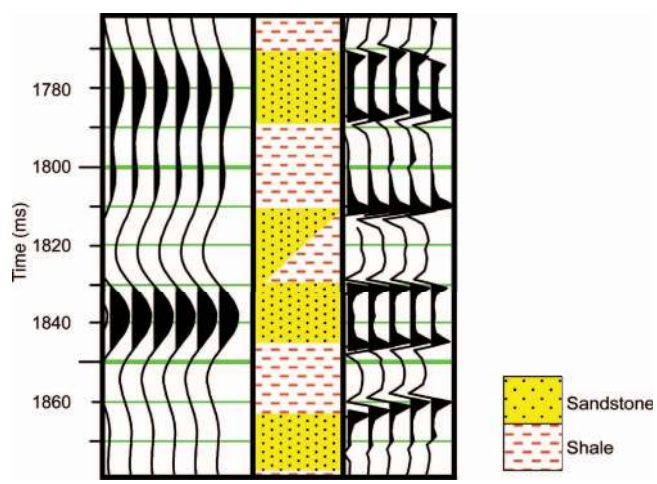

Figure 16. Original seismic data (left) compared with the lithologic column (center) and the thickness inverted data (right). Both images are phase-rotated by $-90°$. Note the failure of the original seismic data to delineate thin layering as compared with the inverted data. Also note that the inverted data do not resolve gradational changes within an individual layer.

Downloaded 02 Sep 2010 to 98.201.156.213. Redistribution subject to SEG license or copyright; see Terms of Use at http://segdl.org/

Thickness comparison

We quantitatively compared thicknesses from the well-log data to those from the spectral reflectivity inversion, interpreting the layering from the well-log data, which were stretched from depth to time on the original synthetic, and comparing the results to the inverted thicknesses as defined by zero crossings on the $-90°$ phase-rotated spectral reflectivity inversion.

We performed the interpretation between 1700 and 2900 ms. The comparison is plotted in Figure 17, with excellent correlation between well-log data thicknesses and the predicted thicknesses (pink) below the tuning line (red). The mean error for the two data sets is $\mu = -0.5$ ms, indicating that the method is generally accurate and unbiased. The square of the correlation coefficient is $R^2 = 0.94$ with a standard deviation of $\sigma = 3.10$ ms, corresponding to precision in thickness estimation on the order of 15 ft (4.5 m) for this example.

Stratigraphic interpretation

Figures 18–20 show stratigraphic examples in which both the original seismic data and the spectrally inverted data have a $-90°$ phase to highlight layer boundaries.

An example of the wavelet overprint effect is observed on the large-scale seismic line comparison of Figure 18. On the original seismic line, an apparent discontinuity is inferred at about 1315 ms (Figure 18a). The discontinuity might be interpreted as a localized fault with minimal offset or as a stratigraphic discontinuity in layering. However, comparison with the inverted data (Figure 18b) reveals another picture. Although the inverted data show more detail in general, the apparent discontinuity in layering does not exist on the inverted section despite the fact that the inverted data are generated using a trace-by-trace operation that makes no assumption about lateral continuity.

On the inverted section, the apparent disruption in layering actually represents a lateral change of rock properties within a given layer. The discrepancy points to the apparent discontinuity in reflection arrival times seen on the original data; it is not a geologic feature but a geophysical effect. Specifically, it is a shift in the wavelet-interference pattern caused by an impedance change that resembles a small geologic layering discontinuity in the seismic image.

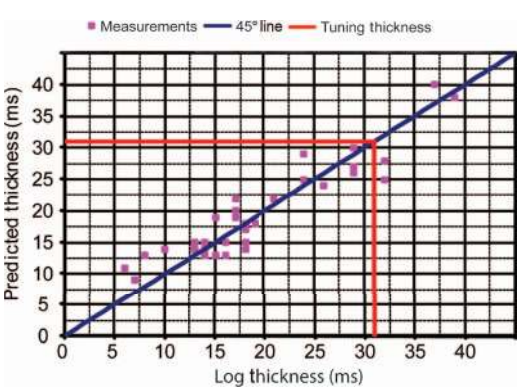

Figure 17. Plot of predicted thicknesses from the inversion (pink squares) versus well-log interpreted thickness (blue line is a 1:1 diagonal), showing a strong correlation between the two. The thicknesses were interpreted between 1700 and 2900 ms. The tuning thickness is marked by the red line, and accuracy is maintained below one-eighth of a wavelength.

The smaller-scale image in Figure 19 shows significant lateral breaks in layering that might be interpreted as discrete sand bodies with possible erosion of previously continuous layers. These features can be caused by different types of downslope transport mechanisms such as channel incision. The horizons on the original data (Figure 19a) are difficult to continue in places (black arrows). How-

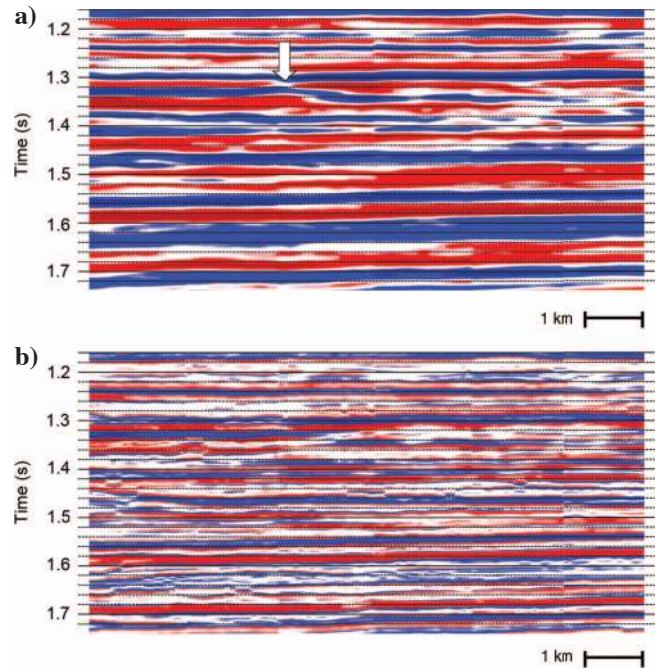

Figure 18. (a) The original seismic data show a small discontinuity. (b) The thickness-inverted data reveal a strikingly continuous layer, a strong indication that the geologic discontinuity seen in (a) is a wavelet effect rather than a real subsurface feature. The phase for both images in $-90°$, and red indicates higher impedance.

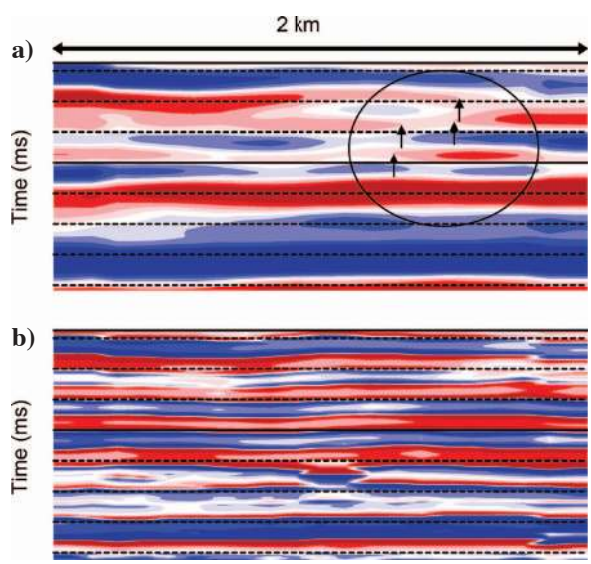

Figure 19. (a) The original seismic line has significant stratigraphic discontinuities (black arrows) that might be interpreted as the termini of discrete depositional lobes. (b) The spectrally inverted data reveal a laterally continuous layering characteristic of undisturbed layer-cake geology. The phase on both images is $-90°$. Timing lines are 20 ms, and red indicates higher impedance.

Downloaded 02 Sep 2010 to 98.201.156.213. Redistribution subject to SEG license or copyright; see Terms of Use at http://segdl.org/

ever, the spectrally inverted data (Figure 19b), which assume no relationship between neighboring traces, show striking continuity along the same horizons. Once again, the complex wavelet-interference pattern creates an illusory geologic scenario that accompanies limited resolution.

The previous examples demonstrate artifacts that resemble geology, and Figure 20 shows an example of the same wavelet effect erasing geologic information. In the original seismic data (Figure 20a), the apparent pinch-out of a low-impedance layer is observed, with the upper and lower events merging below the resolution of the layer (white arrow). However, the spectrally inverted data (Figure 20b) show the same low-impedance layer imaged much farther updip, together with the resolved bounding layers. In addition, an apparent localized broadening or bulge in the wavelet in the original data just below the first two timing lines is resolved as a possible erosional incision on the inverted data. Such improved detection of stratigraphic variation has significant implications for better reservoir characterization and delineation.

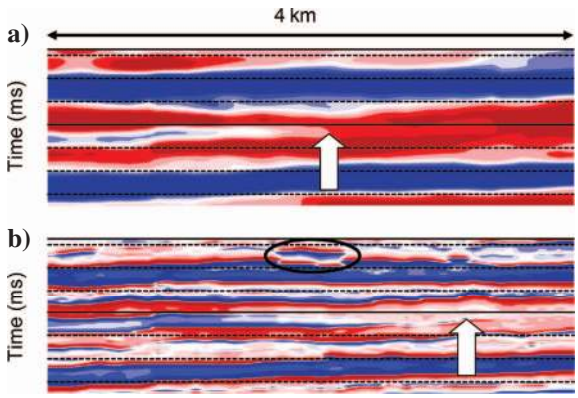

Figure 20. (a) The original seismic data shows a pinch-out (white arrow) where the thin layer becomes unresolved. (b) The inverted data images the pinch-out much farther updip. An apparent erosional feature (black circle) is resolved on the inversion. The phase on both images is $-90°$. Timing lines are 20 ms, and red indicates higher impedance.

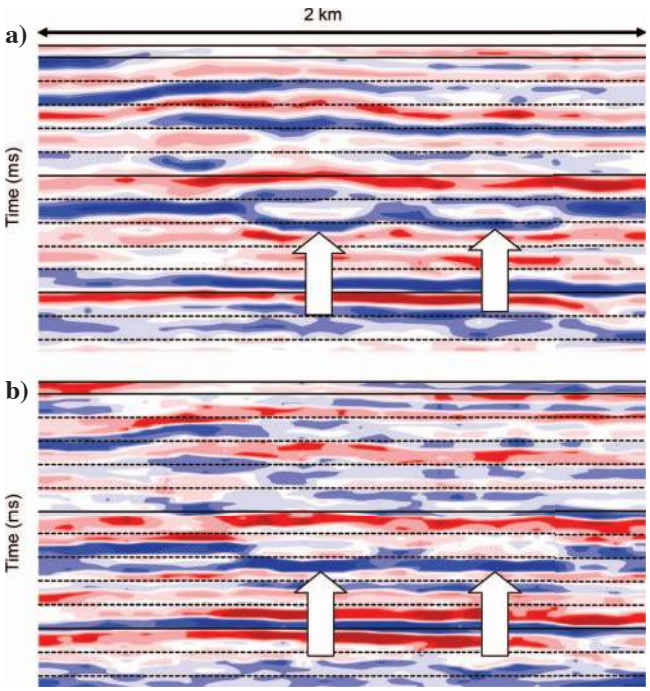

Figure 21. Comparison of (a) the original zero-phase seismic data with (b) the spectrally inverted data, which are phase-rotated $-90°$ from (a). Channels (white arrows show the base of channels) have more relief and more curvature on the original seismic data. Timing lines are 10 ms, and red indicates higher impedance.

We tested the method on a line of data from a shallow Gulf of Mexico data set with known large incision features, previously mapped using the coherence attribute. Figures 21 and 22 show zero-phase original seismic images and $-90°$ phase-rotated spectral-inversion images. Typically, seismic images of channels show significant relief from the levy to the thalweg, which appeals to the intuitive concept of a curved-channel geometry.

Figure 21a is an example of a pair of adjacent channels, showing a strongly curved geometry on the original seismic data. The $-90°$ phase-rotated spectrally inverted section of the data (Figure 21b) shows an alternative image of the channels in which the curvature seen in the channel profile is less prominent, hinting at the possibility that some component of the curvature can be attributed to the rapid rock-property changes known to occur across the strike of a channel. We believe further investigation of this phenomenon using well control is warranted.

Figure 22 shows another large channel imaged on the original seismic data and on the $-90°$ phase-rotated spectral inversion, re-

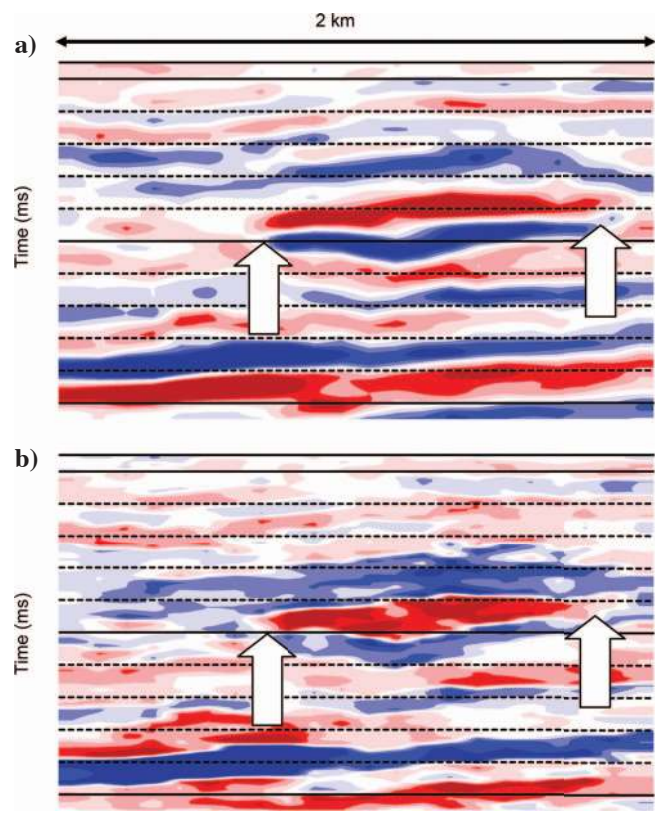

Figure 22. A large channel (white arrows show the edges of the channel) imaged on (a) the original zero-phase seismic data and (b) the spectrally inverted data, which are phase-rotated $-90°$ from (a). The thin-bed layering of the channel edges and overall vertical channel extent are imaged more precisely on the inverted data. Timing lines are 10 ms, and red indicates higher impedance.

Downloaded 02 Sep 2010 to 98.201.156.213. Redistribution subject to SEG license or copyright; see Terms of Use at http://segdl.org/

spectively. The tuning effect in the original data confounds channel-thickness interpretation as the channel thins toward the levies. There is also an ambiguity in the placement of the top and base bounding surfaces of the channel related to the wavelet phase. The inverted data show a clearer picture of the channel geometry, with constant thinning of the channel-fill wedges toward the edges of the channel. In addition, the top and base bounding surfaces of the channel can be picked more precisely on the inverted data at the sharply defined zero crossings with less guesswork in the placement of horizons.

Thus, in the workflow of seismic interpretation, spectral inversion adds visual information that can contribute to delineating geologic features of interest such as channels.

CONCLUSIONS

Beginning with a generalized theory of reflectivity, spectral decomposition is used as a tool to unravel the complex interference patterns created by thin-bed reflectivity. These patterns can be inverted to obtain the original reflectivity. We developed and studied new analytical methods for spectral inversion based on complex spectral analysis. Spectral inversion yields accurate thickness determinations below tuning, using the inverse relationship between thickness and the constant periodicity of spectral interference patterns.

Representing the seismogram as a superposition of simple layer responses constitutes a means of imposing on the inversion the a priori assumption that sedimentary rocks occur as layers with discrete interfaces at the top and base and can be represented as such in a reflectivity series. When this assumption is valid, the consequence is that on the inverted reflectivity trace, there is geologically meaningful information at frequencies outside the band of the original seismic data. When this assumption is false, the recovered frequency information outside the band of the original seismic data will also be false. For example, smooth impedance transitions will be inverted as blocky steps in impedance.

Spectral shape information obtained from spectral decomposition can be used to drive an inversion with significantly greater vertical resolution than that of the original seismic data, thereby improving thickness estimation, correlation to well logs, and stratigraphic interpretation. These results are achieved without using well-log information in the inversion as a starting model or as a constraint. The resulting inversion therefore is unbiased by preconceived ideas. As evidenced by the results of applying the method to real data, spectral inversion has great potential as a practical tool for seismic exploration.

The spectral-inversion methods described in this work demonstrate improvement in vertical resolution; however, we did not use well-log information after the wavelet-removal step. It is desirable to investigate the effectiveness of using well-log data to further improve vertical resolution of interbedded layers or gradational changes within layers that are not revealed by seismic spectral inversion alone. In addition, thickness constraints from spectral inversion could be used as input for more accurate model-based impedance inversion.

ACKNOWLEDGMENTS

The authors would like to thank Gene Sparkman, Carlos Moreno, Xianhui Zhu, and Oleg Portniaguine of Fusion Petroleum Technologies for their help and support. Thanks also to Kurt Marfurt and Scott Morton for assistance, suggestions, and contributions. Financial support was provided by ExxonMobil and Shell.

APPENDIX A

THE SHIFT EFFECT

When examining the real and imaginary components separately, a phase shift occurs if the analysis window is not centered on the layer. To study this effect in more detail, we revisited the original equations. The shift theorem says that a time sample shift Δt away from the layer center t_c in the time domain is equivalent to a phase ramp in the frequency domain:

$$g(t_c + \Delta t) \leftrightarrow e^{2i\pi f\Delta t} g(f). \tag{A-1}$$

Applying this equivalency,

$$e^{2i\pi f\Delta t} g(f) = [\cos(2\pi f\Delta t) + i\sin(2\pi f\Delta t)][2r_e\cos(\pi fT) + i2r_o\sin(\pi fT)]. \tag{A-2}$$

Taking the real component of equation A-2,

$$\mathrm{Re}[e^{2i\pi f\Delta t} g(f)] = 2r_e\cos(\pi fT)\cos(2\pi f\Delta t) - 2r_o\sin(\pi fT)\sin(2\pi f\Delta t). \tag{A-3}$$

Rearranging yields

$$\begin{aligned}\mathrm{Re}[e^{2i\pi f\Delta t} g(f)] &= 2r_o[\cos(\pi fT)\cos(2\pi f\Delta t) - \sin(\pi fT)\sin(2\pi f\Delta t)] \\ &\quad + 2(r_e - r_o)\cos(2\pi f\Delta t)\cos(\pi fT), \\ &= 2r_o\cos(2\pi f(\Delta t + T/2)) + 2(r_e - r_o)\cos(2\pi f\Delta t)\cos(\pi fT),\end{aligned} \tag{A-4}$$

which has the form of a modulation and represents the spectral plots of time-shifted models. A similar expression can be derived for the odd component. The phase shift corresponds to a sinusoidal modulation of the signal, which can be viewed as an interference pattern superimposed on another interference pattern. Furthermore, the period of the interference pattern is determined by the magnitude of the shift.

APPENDIX B

INVERSION-MODEL DERIVATION

Applying the shift theorem (equation A-1) and taking general expressions for the real and imaginary spectra,

$$\mathrm{Im}[e^{2i\pi f\Delta t} g(f)] = 2r_o\sin(\pi fT)\cos(2\pi f\Delta t) + 2r_e\cos(\pi fT)\sin(2\pi f\Delta t) \tag{B-1}$$

and

Downloaded 02 Sep 2010 to 98.201.156.213. Redistribution subject to SEG license or copyright; see Terms of Use at http://segdl.org/

$$\mathrm{Re}[e^{2i\pi f\Delta t}g(f)] = 2r_e\cos(\pi fT)\cos(2\pi f\Delta t) - 2r_o\sin(\pi fT)\sin(2\pi f\Delta t). \tag{B-2}$$

Expressing the amplitude spectrum and setting $\Delta t = 0$ as a constant reference,

$$G(f) = \sqrt{\{\mathrm{Re}[e^{2i\pi f\Delta t}g(f)]\}^2 + \{\mathrm{Im}[e^{2i\pi f\Delta t}g(f)]\}^2} = \sqrt{4r_e^2\cos^2(\pi fT) + 4r_0^2\sin^2(\pi fT)}. \tag{B-3}$$

Rearranging terms,

$$G(f) = 2\sqrt{(r_e^2 - r_0^2)\cos^2(\pi fT) + r_0^2\cos^2(\pi fT) + r_0^2\sin^2(\pi fT)}. \tag{B-4}$$

Taking the derivative,

$$\frac{dG(f)}{df} = -\frac{2\pi T(r_e^2 - r_o^2)\cos(\pi fT)\sin(\pi fT)}{\sqrt{(r_e^2 - r_o^2)\cos^2(\pi fT) + r_0^2}}. \tag{B-5}$$

Multiplying and simplifying using trigonometric identities yields

$$G(f)\frac{dG(f)}{df} = -4\pi T(r_e^2 - r_0^2)\cos(\pi fT)\sin(\pi fT) = -2\pi Tk\sin(2\pi fT), \tag{B-6}$$

where $k = r_e^2 - r_o^2$.

NOMENCLATURE

Variable	Definition
t	Seismic record time
$g(t)$	Time-domain impulse pair
r_1	Top reflector in a two-reflector model
r_2	Base reflector in a two-reflector model
t_1	Time at top reflector in a two-reflector model
t_2	Time at base reflector in a two-reflector model
T	Layer two-way traveltime thickness
t_c	Time at layer center in a two-reflector model
Δt	Time shift
f	Frequency
$g(f)$	Frequency-domain impulse response
Re	Real component of a function
Im	Imaginary component of a function
r_e	Even component of the reflection coefficient
r_o	Odd component of the reflection coefficient
$G(f)$	Magnitude of amplitude as a function of frequency
$dG(f)/df$	Derivative of magnitude of amplitude with respect to frequency
k	Even component of reflectivity squared minus odd component squared
t_R	Tuning thickness
f_o	Wavelet peak frequency
$r(t)$	Reflection-coefficient series as a function of time
τ	Convolutional placeholder
II	Even impulse pair
I_I	Odd impulse pair
$s(t,f)$	Time- and frequency-varying seismic trace
$w(t,f)$	Time- and frequency-varying seismic wavelet
t_w	Window half-length
$O(k,T)$	Frequency-varying objective function
$O(t,r_e,r_o,T)$	Time- and frequency-varying objective function
α_e	Even-component weighting function
α_o	Odd-component weighting function
f_L	Low-frequency cutoff
f_H	High-frequency cutoff

REFERENCES

Castagna, J. P., 2004, Spectral decomposition and high resolution reflectivity inversion: Presented at the Oklahoma Section Meeting, SEG, ⟨wildhorse.insinc.com/cseg/castagna/⟩.

Castagna, J. P., S. Sun, and R. W. Siegfried, 2003, Instantaneous spectral analysis: Detection of low-frequency shadows associated with hydrocarbons: The Leading Edge, **22**, 120–127.

Chopra, S., J. P. Castagna, and O. Portniaguine, 2006a, Seismic resolution and thin-bed reflectivity inversion: Canadian Society of Exploration Geophysicists Recorder, **31**, 19–25.

———, 2006b, Thin-bed reflectivity inversion: 75th Annual International Meeting, SEG, Expanded Abstracts, 2057–2061.

Chung, H., and D. C. Lawton, 1995, Frequency characteristics of seismic reflections from thin beds: Canadian Journal of Exploration Geophysicists, **31**, 32–37.

Kallweit, R. S., and L. C. Wood, 1982, The limits of resolution of zero-phase wavelets: Geophysics, **47**, 1035–1046.

Marfurt, K. J., and R. L. Kirlin, 2001, Narrow-band spectral analysis and thin-bed tuning: Geophysics, **66**, 1274–1283.

Partyka, G. A., 2005, Spectral decomposition: SEG Distinguished Lecture, ⟨http://ce.seg.org/dl/spring2005/partykaabstract.shtml⟩.

Partyka, G. A., J. A. Gridley, and J. A. Lopez, 1999, Interpretational aspects of spectral decomposition in reservoir characterization: The Leading Edge, **18**, 353–360.

Portniaguine, O., and J. P. Castagna, 2004, Inverse spectral decomposition: 74th Annual International Meeting, SEG, Expanded Abstracts, 1786–1789.

———, 2005, Spectral inversion: 75th Annual International Meeting, SEG, Expanded Abstracts, 1638–1641.

Puryear, C. I., 2006, Modeling and application of spectral inversion for determination of layer properties: M.S. thesis, University of Houston.

Puryear, C. I., and J. P. Castagna, 2006, An algorithm for calculation of bed thickness and reflection coefficients from amplitude spectrum: 76th Annual International Meeting, SEG, Expanded Abstracts, 1767–1770.

Tirado, S., 2004, Sand thickness estimation using spectral decomposition: M.S. thesis, University of Oklahoma.

Widess, M., 1973, How thin is a thin bed?: Geophysics, **38**, 1176–1180.

Downloaded 02 Sep 2010 to 98.201.156.213. Redistribution subject to SEG license or copyright; see Terms of Use at http://segdl.org/